Kovove Mater. 64 2026 133–147
DOI: 10.31577/km.2026.3.133

In-situ gradient Ti(C,N) in AlCoCrFeNi high entropy alloy coatings by laser cladding technology with electromagnetic fields

Yanjun Xi[1], Hao Wang[1], Mingxing Ma[1,2]*, Lujun Cui[1]

[1] *School of Materials Electronics and Energy Storage, Zhongyuan University of Technology, Zhengzhou 451191, P. R. China*
[2] *School of Mechanical Engineering, Henan Polytechnic Institute, Nanyang 473000, P. R. China*

Received 27 February 2026, received in revised form 6 June 2025, accepted 11 June 2026

Abstract

Electromagnetic field-assisted laser cladding technology was employed successfully to prepare in-situ gradient Ti(C,N) in AlCoCrFeNi high entropy alloy coatings. The microstructure, elemental and phase distributions were investigated by SEM and XRD. The microhardness, wear resistance, and electrochemical corrosion behavior were studied. The results revealed that a gradient distribution of micro hardness from the substrate to coating was achieved when introducing the electromagnetic field, due to the gradient distribution of the Ti(C,N) ceramic phase. The gradient coating greatly improves the corrosion resistance of the material in 3.5% NaCl solution because more ceramic phases are formed on the surface to hinder the electron transfer during corrosion. A corrosion model has been created to better understand the corrosion mechanism of different composite coatings.

K e y w o r d s: gradient coating, electromagnetic field, laser cladding; high entropy alloy

1. Introduction

High entropy alloy (HEA) is a type of alloy composed of five or more metallic and non-metallic elements in equimolar or near-equimolar ratios, forming a simple solid solution structure [1, 2]. These alloys have a special microstructure and excellent properties, such as high strength, wear resistance, corrosion resistance, excellent strength and toughness, and good thermal stability and oxidation resistance [3–5], which makes them a research hotspot.

AlCoCrFeNi is a typical equiatomic HEA, which was one of the HEAs studied earliest due to its excellent heat resistance and outstanding mechanical properties [6, 7]. Laser cladding is recognized as the superior surface technique due to its rapid deposition rate and low heat input [8, 9]. Laser-clad high-entropy alloy coatings have garnered widespread attention because of the excellent wear resistance and corrosion resistance [10–16]. To further enhance the hardness and wear resistance of AlCoCrFeNi coatings, researchers have directly added ceramic particles into HEA coatings [17–21]. However, this approach has certain limitations, such as particle aggregation, susceptibility to microcracking, and poor interfacial bonding [22].

To overcome these limitations, researchers have prepared in-situ ceramic particle-reinforced composite coatings using laser cladding. In-situ ceramic composite coatings have several advantages: (a) Ceramic particles embedded in the composite coatings can exhibit greater thermodynamic stability; (b) the contact area between ceramic particles and the coatings increases, resulting in a clean interface; (c) the size, morphology, and distribution of reinforced particles are more controllable [23].

Although in-situ ceramic-HEA composite coatings show many advantages, excess ceramic within the coating can lead to a significant reduction in bonding performance. The challenge lies in maintaining the bonding performance without sacrificing the benefits of ceramic particles within the coating. Gradient coatings are used in industrial materials based on different deformation mechanisms and preparation processes. They consist of a bonding layer and multiple layers with different ceramic contents, built up through successive deposition [24–26]. However, the intricate pro-

*Corresponding author: e-mail address: manager92@163.com

cess and the presence of multiple coating interfaces can exponentially increase the tendency for defects within the coating.

Compared to the multilayer process of traditional graded coatings, the alignment of non-metallic or metallic particles within liquid metals can be controlled through a designed magnetic field [27]. This can result in magnetic separation, uniform magnetization of solid particles, and redistribution of solutes [28], thereby achieving one-step preparation of gradient coatings. However, in small-sized melt pools, the application of a gradient magnetic field to the coating has significant limitations. It is necessary for the ceramic phases to respond to a high magnetic field gradient [29], which in turn consumes substantial energy. This is detrimental to energy conservation and emissions reduction efforts.

To solve this problem, we introduced an electric field to prepare gradient coatings under a relatively low-intensity uniform magnetic field. This involved perpendicular magnetic and electric fields [30–32]. In conductive liquid melt pools, ceramic particles tend to move in a fixed direction due to the electromagnetic Archimedes force [33, 34]. Huo [33] achieved IN718/WC composite coatings by electromagnetic-assisted laser cladding technology. WC particles precipitated within the IN718/WC composite coatings. However, the electromagnetic field induced upward electromagnetic forces that acted on the reinforcing particles, resulting in uniform distribution within the composite coating. Wang [34] investigated the influence of an electromagnetic filed on the distribution of laser-melt particles through numerical simulations and experimental methods. The results demonstrated that most particles were trapped in the upper region of the laser melt layer when the Lorentz force and gravity were in the same direction. Conversely, when the Lorentz force and gravity opposed each other, most particles concentrated in the lower region. The numerical results were consistent with the experimental results. However, these studies deliberately added ceramic particles into the melt pool. Currently, there is little research on the impact of an electromagnetic field on in-situ ceramic and high-entropy alloy composite coatings prepared by laser cladding.

In the present work, in-situ AlCoCrFeNi-Ti(C,N)

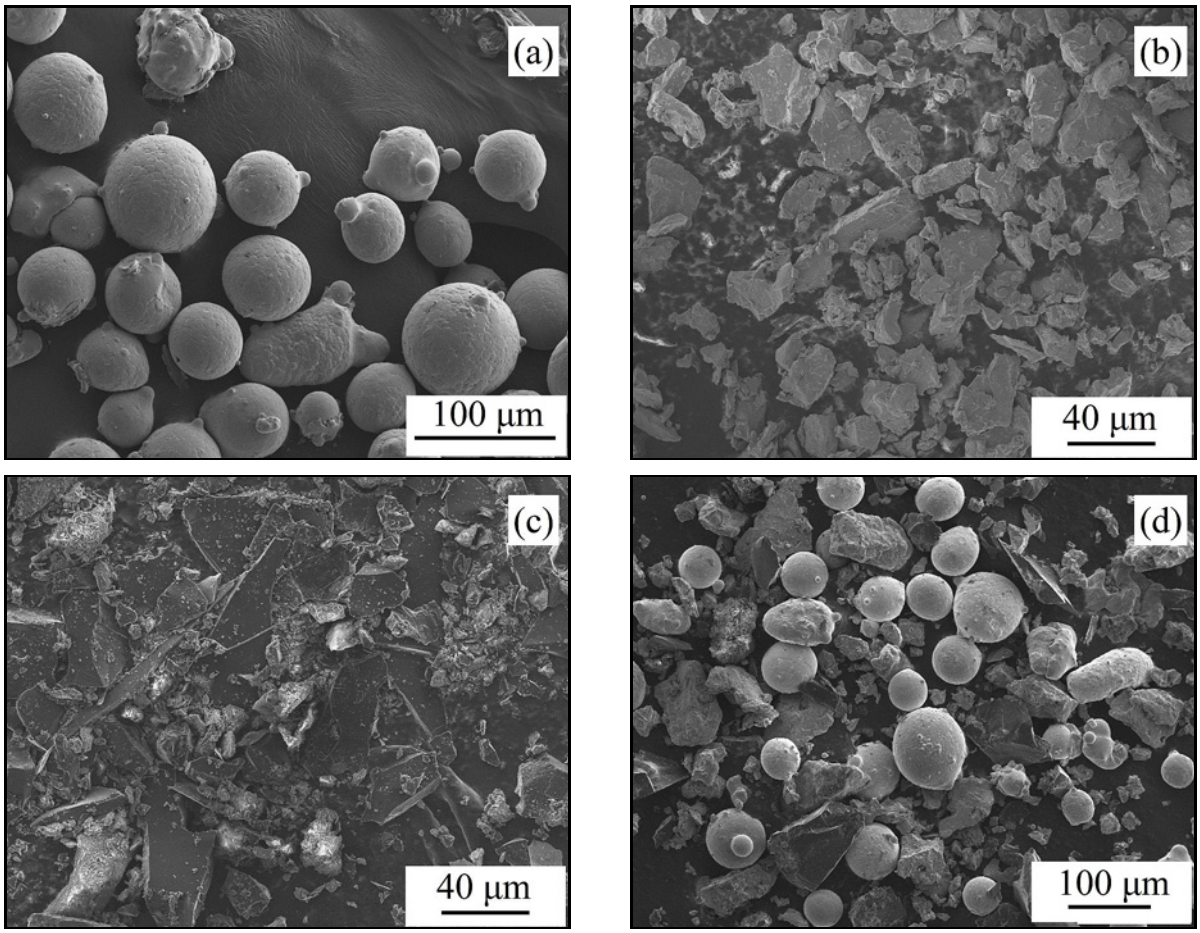

Fig. 1. SEM morphology of powders: (a) AlCoCrFeNi powder, (b) Ti particles, (c) B_4C particles, and (d) mixed powder.

composite coatings were prepared on 304 stainless steels by electromagnetic field-assisted laser cladding technology. By adjusting the electric field and magnetic field, a series of AlCoCrFeNi-Ti(C,N) coatings were achieved. The influence of the electromagnetic field on the microstructure and phases was investigated by scanning electron microscopy (SEM) with energy-dispersive spectrometry (EDS) and X-ray diffraction (XRD). Microhardness was studied using a digital microhardness tester, and the corrosion behavior of the composite coatings in 3.5 wt.% NaCl solution was evaluated. It is particularly important to point out that a model of electromagnetic field-assisted laser cladding has been developed to better understand the coating preparation process. Moreover, corrosion model has been created to better understand the corrosion mechanism of different composite coatings.

2. Materials and methods

2.1. Material preparation

AISI 304 stainless steel with dimensions of 100 mm × 30 mm × 10 mm was prepared as the substrate. Figure 1a shows the morphology of AlCoCrFeNi HEA powder. The AlCoCrFeNi powder was spherical, 53 to 150 μm in size. The particle size ranges from 30 to 50 μm for Ti powder and from 45 to 60 μm for B_4C, both of which were aspherical. Figures 1b,c show the morphology of Ti and B_4C particles. AlCoCrFeNi powder, Ti powder and B_4C powder were mixed in a mass ratio of 26 : 10 : 4, and protective gas N_2 was provided. Figure 1d shows the morphology of the mixed powder consisting of AlCoCrFeNi, B_4C, and Ti particles. After mixing, the three kinds of particles were distributed evenly without obvious agglomeration.

2.2. Experimental procedure

Prior to laser cladding, the 304 stainless steel substrate was prepared by grinding and polishing with 600# WC paper to remove the oxide layer. Subsequently, it was degreased using anhydrous ethanol and subjected to ultrasonic cleaning. The blended powder was then introduced into a planetary ball mill along with stainless steel grinding balls of 5–25 mm diameter, in an argon-filled environment. The ball-to-powder ratio was set at 4 : 1, and the milling speed was maintained at 400 r min^{-1}. The uniformly mixed powder was dried at 80 ℃ in a vacuum drying chamber (DZF-6050) for 2.5 h. Polyvinyl alcohol adhesive was then added to the dried coating powder, followed by thorough stirring until a homogeneous paste is attained. Utilizing a custom-designed mold within a hydraulic press under a load of 10 kN, the paste was compacted onto the substrate to form a precoating with dimensions of 80 mm × 24 mm × 2 mm. The sample was then subjected to drying for 24 h within a vacuum drying chamber at 100 ℃.

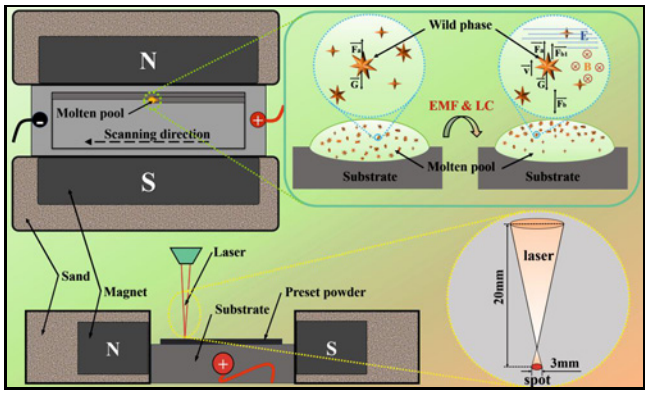

Fig. 2. Schematic diagram of laser cladding assisted by electromagnetic field.

Table 1. Processing parameters of laser cladding

Laser power (W)	800
Scanning speed (mm min^{-1})	300
Spot diameter (mm)	3
Scanning distance (mm)	20
Overlap rate (%)	30

Table 2. Experimental conditions of specimens

Experimental group	Sample A	Sample B	Sample C	Sample D
Magnetic field (T)	0	0.8	0.8	0.8
Direct current (A)	0	0	3	3
Electric field direction	–	–	+1	–1

The schematic diagram of the electromagnetic field designed by our project team is illustrated in Fig. 2. The magnetic field was generated by several NdFeB magnets each of size of 80 mm × 20 mm × 10 mm each. The magnetic flux density in the melt pool ranged from 0.8 to 1 T, as measured by a handheld digital tesla meter (TD8620). A stable electric field was supplied by a dual-channel trackable DC power supply (DC1712A, China). During laser cladding, the current density was maintained at 3 A mm^{-2}.

A 4kW laser 3D printer (LDM8060, RAYCHAM, China) was utilized to prepare the coating. The machining parameters are detailed in Table 1. To comprehend the impact of the electromagnetic field on the AlCoCrFeNi/Ti(C,N) composite coating, composite coatings were prepared under different magnetic and electric fields, as shown in Table 2. Sample A

was prepared without an electromagnetic field. Sample B was prepared with a magnetic field only. Sample C (electromagnetic force downward) and sample D (electromagnetic force upward) were prepared with an electromagnetic field.

2.3. Microstructure observation

After obtaining the coating, the samples were cut vertical to the laser scanning direction using wire electrical discharge machining equipment. Subsequently, the samples were ground, polished and etched using aqua regia. The morphological and microstructural characteristics of the material were examined using a scanning electron microscope (SEM), a Zeiss Merlin Compact field emission scanning electron microscope (FESEM) with an energy-dispersive X-ray spectroscopy (EDS) system. X-ray diffraction (XRD) was employed to study the phase formation of the coating. The specific parameters are as follows: copper target X-rays, tube voltage of 40 kV, tube current of 40 mA, scanning speed of $5° \, min^{-1}$, scan-

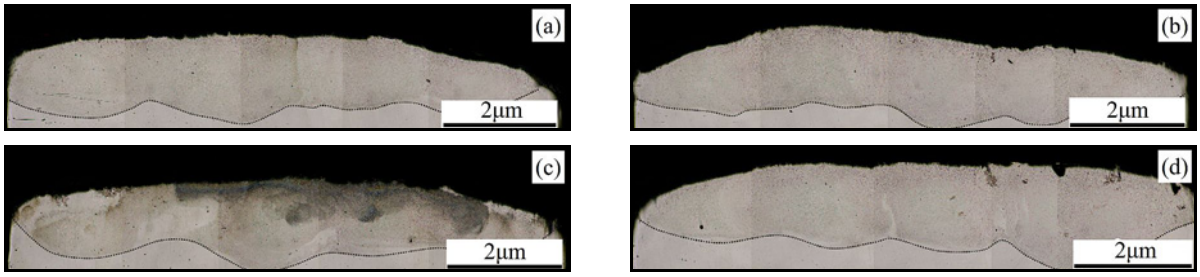

Fig. 3. SEM morphology of AlCoCrFeNi-Ti(C,N) coatings: (a) sample A, (b) sample B, (c) sample C, and (d) sample D.

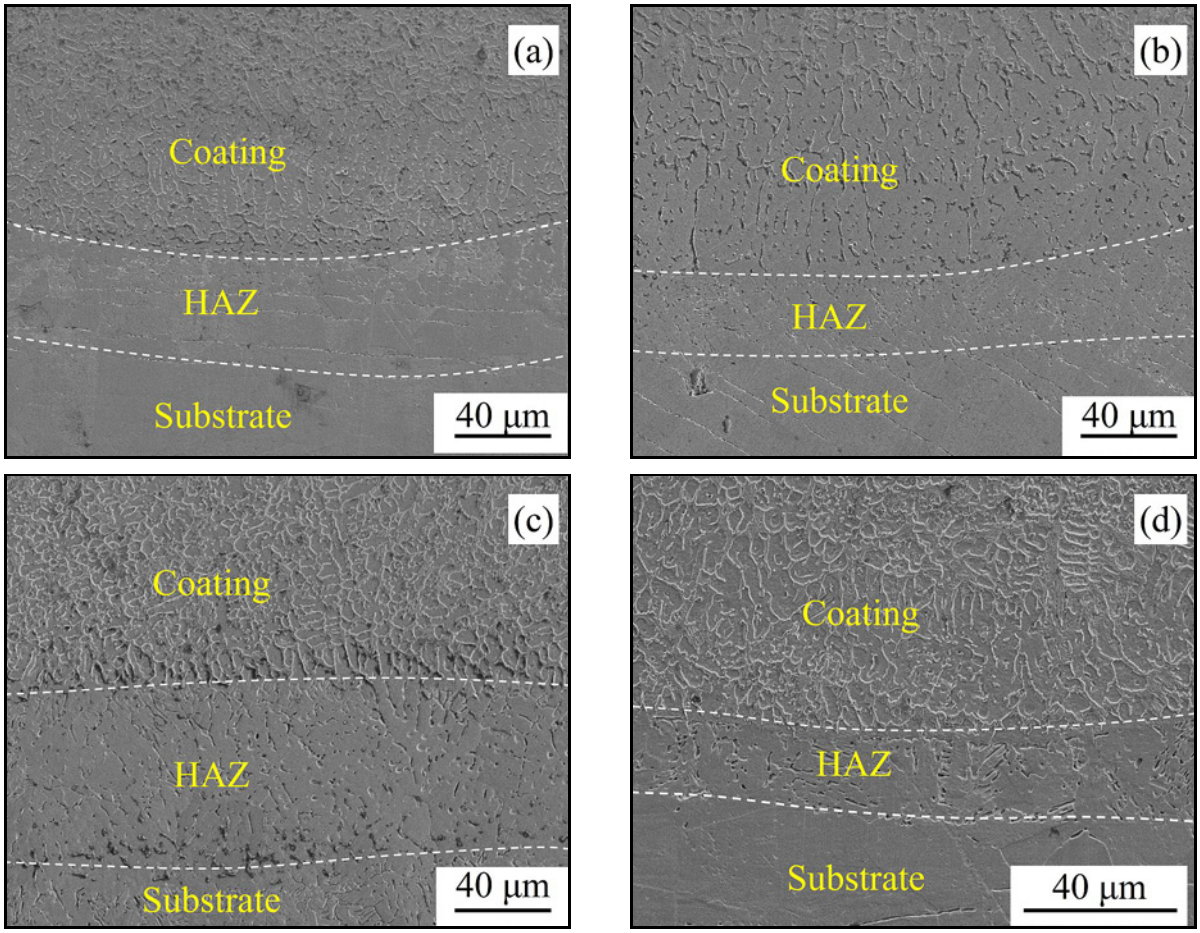

Fig. 4. Cross-sectional microstructure of the AlCoCrFeNi-Ti(C,N) coatings: (a) sample A, (b) sample B, (c) sample C, and (d) sample D.

ning range from 20° to 90°, and a step size of 0.02°.

2.4. Hardness and wear resistance

Microhardness measurements were conducted using a YQ-C1000Z digital micro hardness tester. The experimental load applied was 300 g. The loading time for the indenter was set at 10 s. Microhardness was measured at intervals of 200 µm from the coating surface to the substrate. At the same depth within the specimen, five different points were measured. The maximum and minimum values were excluded, and the average of the remaining three values was considered as the average microhardness for that particular position.

The friction and wear performance were studied using a friction and wear testing machine (RTEC-2816, USA). GCr15 steel was selected as the counterpart material, with a track diameter of 4 mm, a rotation speed of 200 r min^{-1}, and a testing time of 30 minutes. Before testing, the sample was ground and polished. After the test was completed, the wear rate and friction coefficient were obtained.

2.5. Electrochemical test

The corrosion behaviour of the AlCoCrFeNi/Ti(C,N) coating in a 3.5 wt.% NaCl solution was evaluated using an electrochemical workstation (CHI760). A saturated calomel electrode (SCE), a platinum electrode, and a coated specimens served as the reference electrode, auxiliary electrode, and working electrode, respectively. The polarization curve was measured by potentiodynamic scanning at a scan rate of 1 mV s^{-1}. The self-corrosion potential E_{corr} and corrosion current density I_{corr} were obtained by Tafel region extrapolation method. The electrochemical impedance test was carried out in a frequency range of 10^{-2} to 10^{6} Hz, with data fitting conducted using *Z-view software*. The corrosion behaviour was also characterized by electrochemical impedance spectroscopy.

3. Results and discussion

3.1. Microstructure

Figure 3 shows the cross-section morphology of the AlCoCrFeNi-Ti(C,N) coatings on the 304 stainless steel surfaces. It is obvious that the coating is clean, with no porosity, cracks or other defects, indicating good coating quality.

Figure 4 shows the cross-sectional microstructure of the AlCoCrFeNi-Ti(C,N) coatings, which exhibit uniform coatings without defects. The coatings have a metallurgical bond with the substrate, indicating a well-bonded interface. It is easy to observe that the transition zone is widest in coating in Fig. 4c and narrowest in coating in Fig. 4d. In Fig.4c, electromagnetic forces act as a volumetric force within the melt pool, perpendicular to the magnetic field and electric field, and vertically downward, exerting their influence over the entire melt pool. This enhances the downward convection near the solid-liquid interface due to the Marangoni effect, thereby increasing the dilution rate of the coating.

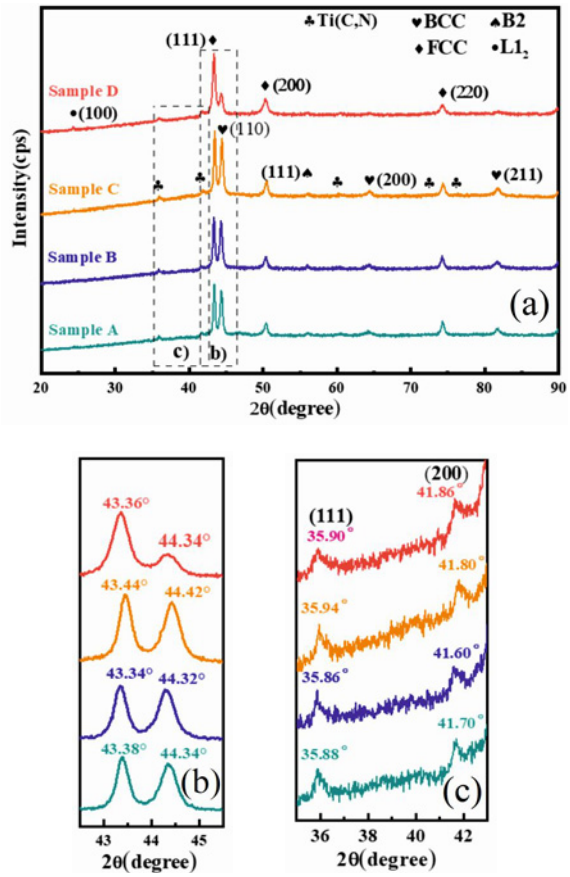

Fig. 5. XRD patterns of AlCoCrFeNi-Ti(C,N) coatings: (a) XRD pattern, (b) magnified line of area b) in figure (a); (c) magnified line of area c) in figure (a).

Figure 5 shows the X-ray diffraction (XRD) patterns of the AlCoCrFeNi-Ti(C,N) coatings. In Fig. 5a, it is observed that the coating is primarily composed of BCC and FCC phases. The disordered BCC (A2) phase typically corresponds to the space group of Im-3m [35, 36] and is rich in Fe and Cr. Additionally, a small amount of the ordered BCC (B2) phase is present, generally corresponding to the space group of Pm-3m, which is rich in Al and Ni. The existence of the B2 phase is confirmed by a small diffraction peak located at 56°, corresponding to the (111) plane. The formation of the FCC phase can be attributed to the excess Fe and Cr present in the AlCoCrFeNi-

-Ti(C,N) coating [37]. During the laser cladding process, Fe, Cr, and C from the substrate are incorporated into the coating structure. As a result, excessive Fe and Cr promote the formation of the FCC phase within the AlCoCrFeNi-Ti(C,N) coating [38–40]. Furthermore, a small amount of the $L1_2$ phase is detected. This is confirmed by a small diffraction peak around 24°, corresponding to the (100) plane of the $L1_2$ phase.

Figure 5b displays the magnified XRD patterns of various samples in the range of 42.5° to 45.5°, corresponding to two diffraction peaks: the (111) plane of the FCC phase and the (110) plane of the BCC(A2) phase. Compared to sample A, which had no applied electromagnetic field, sample B prepared with only a magnetic field exhibits slight small-angle shifts in the positions of both diffraction peaks, although these shifts are minimal. In contrast, sample C prepared with an electromagnetic field shows noticeable large angle shifts in the positions of both diffraction peaks. This is likely due to the downward electromagnetic force acting on the melt pool during cladding. This volumetric force affects the entire melt pool, compressing it and bringing atoms closer together. Consequently, when the melt pool solidifies, fewer small-radius atoms such as boron and carbon remain in the interstitial spaces of the lattice, causing an expansion of the lattice constants and a rightward shift of the peaks. Furthermore, it's observed that the peak intensities have increased, indicating that the downward electromagnetic force promotes an increase in the crystallinity of both the FCC and BCC phases. In sample D, the position of the two diffraction peaks shifts almost back to that of the sample without the electromagnetic field. Additionally, the intensity of the BCC(A2) diffraction peak decreased significantly, indicating that the upward electromagnetic force suppressed the formation of the BCC(A2) phase.

In Fig. 5, the peaks corresponding to the TiC phase (JCPDS 32-1383) and the TiN phase (JCPDS 87-0631) almost completely overlap. This is because both TiC and TiN belong to the cubic crystal system, with TiC having a body-centered cubic structure and TiN having a face-centered cubic structure. Their lattice parameters are similar, resulting in fully coherent diffraction [41]. Consequently, it can be inferred that The Ti(C,N) solid solution is formed. Ti(C,N) grows rapidly along the [100] direction, leading to an unstable interface and the formation of dendritic structures along this direction. The exposed dendrites are predominantly the (111) crystal planes, which have the lowest interfacial energy [42]. The reaction between Ti and B_4C to form TiC is exothermic, leading to a reduction of the temperature gradient in the melt pool and extending the life of the melt pool. This, in turn, provides more transfer and growth time for nitrogen (N) in the Ti(C,N).

The crystal structure of TiC is a face-centered cubic with a NaCl-type arrangement. When N elements are introduced, some C atoms in the TiC lattice are replaced by N atoms, forming a Ti(C,N) solid solution. The crystal structure of Ti(C,N) remains a face-centered cubic of the NaCl type. The atomic radius of C is 0.091 nm, while that of N is 0.075 nm. Because the atomic radius of N is smaller than that of C, lattice contraction occurs when N atoms substitute for C atoms, resulting in a reduction in lattice constants. In comparison to coatings formed without the assistance of an electromagnetic field, the coating assisted by an electromagnetic field exhibits a large angle shift in the diffraction peaks on the (111) and (200) planes of Ti(C,N) phase, as shown in Fig. 5c. This indicates that the addition of the electromagnetic field increases the proportion of N atoms in Ti(C,N). Furthermore, when the electromagnetic force is directed upward (sample D), a decrease in peak intensity can be observed on the (110) surface of BCC (A1) phase, suggesting a significant decrease in crystallinity.

Figure 6 presents SEM micrographs and local magnifications of the microstructures of the AlCoCrFeNi-Ti(C,N) coating. Three distinct microstructures were observed: prominent mesh-like structures, recessed porous structures, and a large number of dispersed gray reinforcement phases. The high-magnification microstructure shows that the grain boundaries are clearly visible. Through EDS analysis, it was determined that the composition of the reinforcement phases consists of Ti, C, and N elements, as illustrated in Figs. 6a–d. According to the EDS analysis, it is evident that the electromagnetic field increases the content of N element in the reinforcement phase according to the EDS analysis, which is consistent with the analysis from XRD patterns.

The morphological characteristics of the reinforcement phase in the coatings under different cladding conditions remain unchanged, displaying blocky and dendritic structures. Furthermore, the central region of the dendritic reinforcement phase consistently exhibits a spherical structure. EDS results showed a phase consisting of 30.41 at.% Al, 64.12 at.% O, and 5.47 at.% C, indicating an Al-rich oxide, identified as Al_2O_3, as shown at point A^+ in sample B. Due to its higher melting point, Al_2O_3 precipitates first during the melt pool cooling process, serving as a nucleation site for the subsequent growth of Ti(C,N) reinforcement phases. Oxygen (O) was introduced from pure Ti powder and air, since titanium readily absorbs oxygen, making oxidation unavoidable.

When an electric field is added on top of the magnetic field, as shown in Fig. 6c, the direction of the electromagnetic force is consistent with that of gravity. Clearly, the grains of the coating are refined when an electromagnetic field is introduced. The originally recessed structures become connected, and the raised mesh-like structures transform into hollow ribbon-like

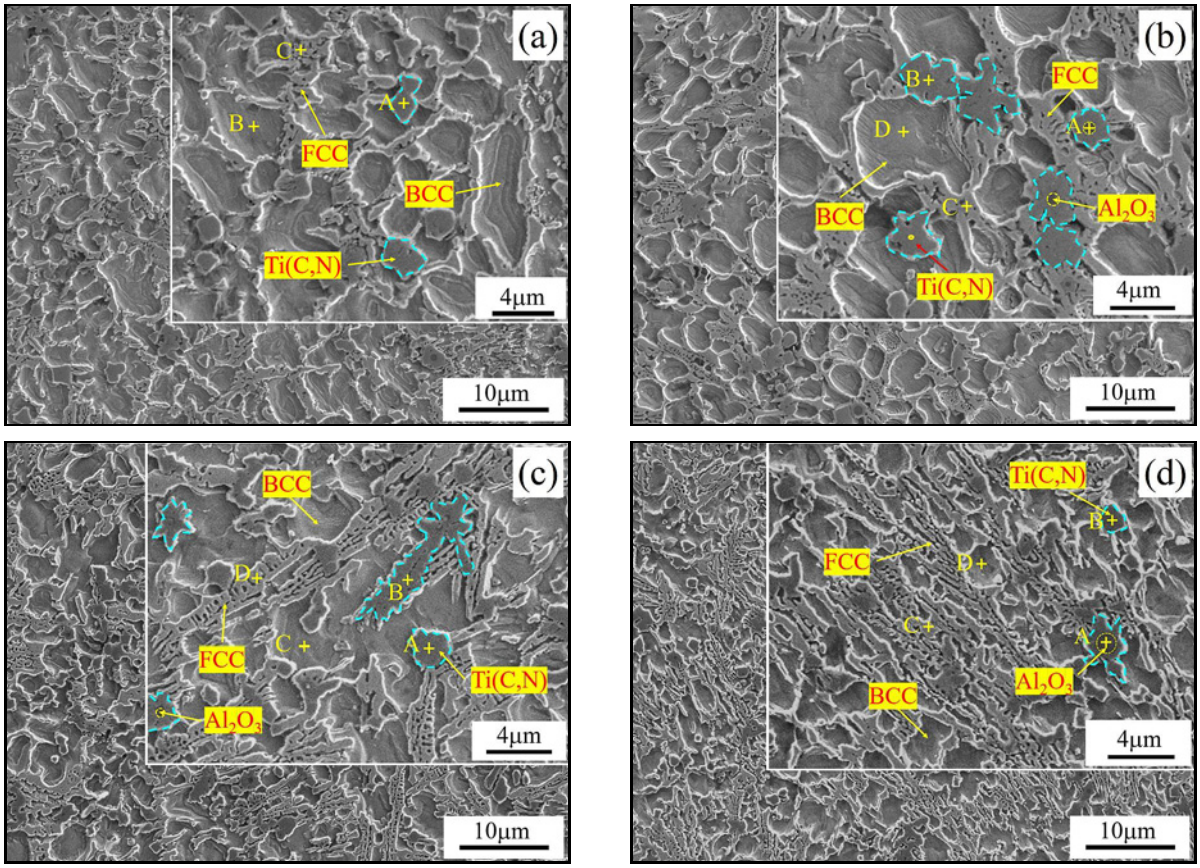

Fig. 6. Microstructure of AlCoCrFeNi-Ti(C,N) coatings: (a) sample A, (b) sample B, (c) sample C, and (d) sample D.

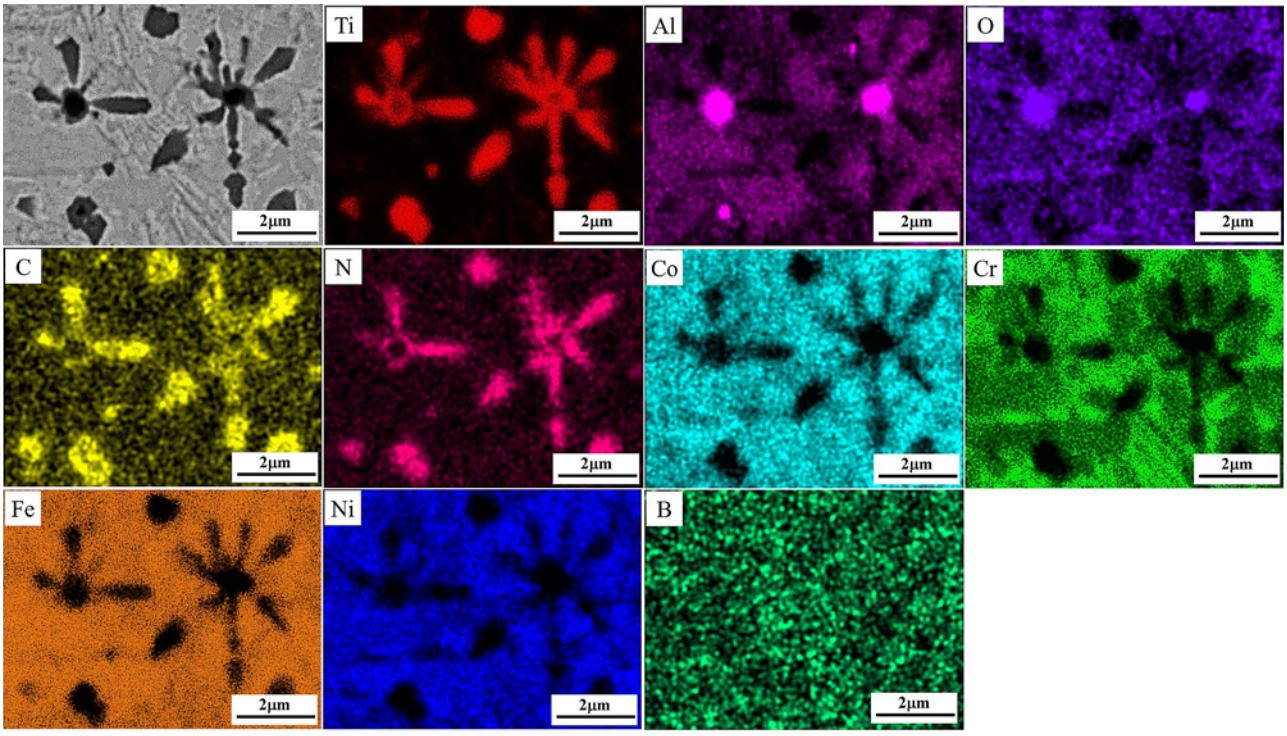

Fig. 7. Elemental mappings of sample C coating.

structures. The structure can be attributed to solute migration induced by electromagnetic forces during directional solidification. This results in uniform distribution of solute, suppressing macro-segregation. In addition, this structure shows orientation, which is more obvious in sample D (Fig. 6d). This might be due to the combined action of electromagnetic stirring to promote flow and the magnetic response of Fe and Ni elements, which collectively inhibit the formation of the BCC structure on the (110) plane [42, 43]. In addition, the size of the recessed structures is smaller, and their area proportion is reduced. This is because the electromagnetic field can increase the phase transformation driving force (similar to increasing subcooling), leading to an increased nucleation rate. Consequently, the growth rate of the BCC phase decreases, leading to grain refinement [44], as observed in the XRD analysis in Fig. 5b.

Figure 7 presents the elemental distribution map of sample C by TM4000plus. Elements such as Co,

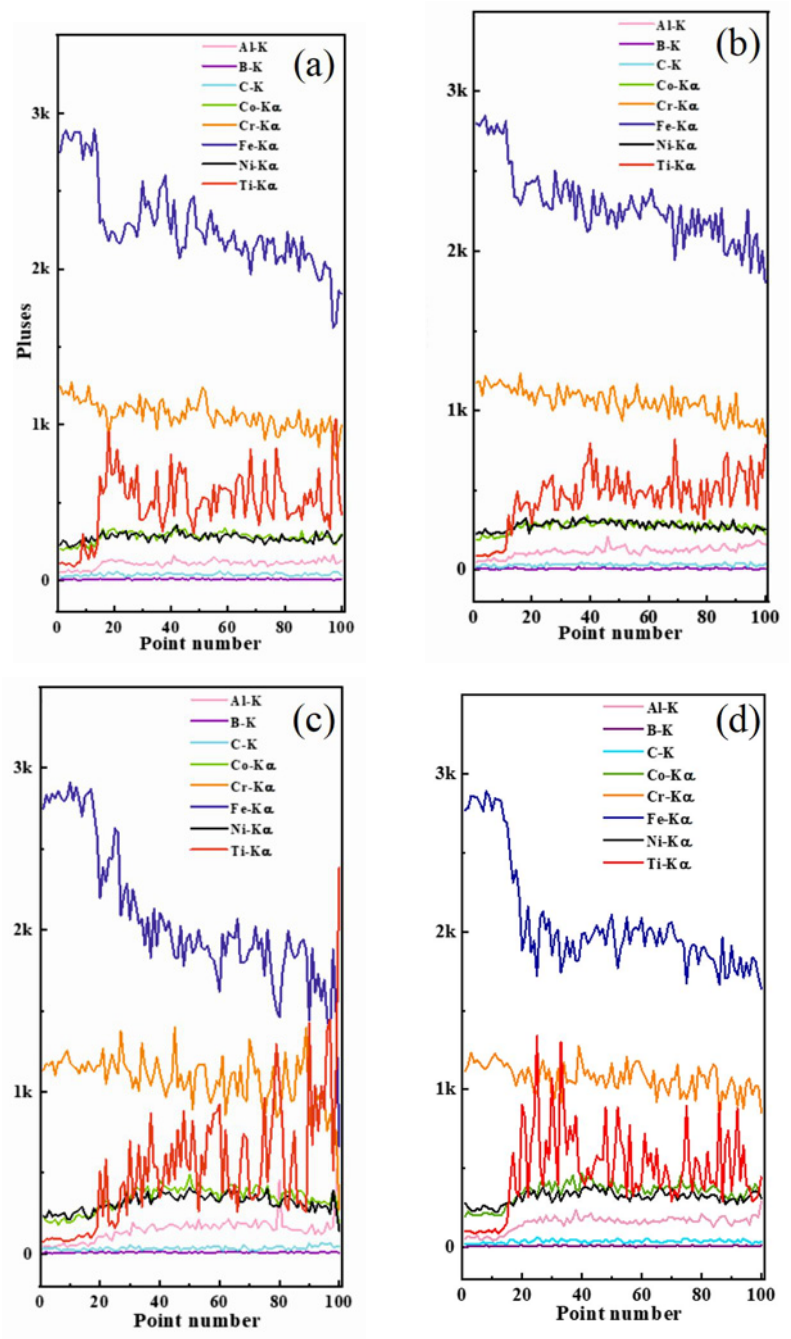

Fig. 8. EDS line scan analysis of AlCoCrFeNi-Ti(C,N) coating: (a) sample A, (b) sample B, (c) sample C, and (d) sample D.

Fe, and Ni exhibit uniform distribution without segregation. The areas enriched in Cr exhibit darker, and the areas enriched in Al are lighter. This result is consistent with the previous EDS analysis. Al and O elements are enriched in the core, while Ti, C, and N elements are distributed on the flower-shaped and circular reinforcing phases, tightly surrounding the spherical Al_2O_3. Because the content of element B in the inner layer is relatively low, it is almost undetectable.

Figure 8 shows EDS line scan analysis from the substrate to the surface. A notable variation in the proportion of Ti is observed with the addition of the electromagnetic field. Figure 8c shows the EDS features on the coating with electromagnetic force parallel to gravity (sample C). There is a gradient distribution of Ti, whose contents increase from the interface to the surface gradually and reach the peak near the surface. When the electromagnetic force opposes to the gravity, the Ti element distribution is reversed, as shown in Fig. 8d. It indicates that the electromagnetic field can control the gradient distribution of the reinforcing phase Ti(C,N), successfully achieving the preparation of functional gradient coatings.

3.2. Microhardness and wear resistance results

Figures 9a,b show the microhardness from the substrate to the surface for the AlCoCrFeNi coating and the AlCoCrFeNi-Ti(C,N) coating, respectively. The preparation processes of samples A0, B0, C0, and D0 were consistent with that of samples A, B, C, and D, respectively.

In Fig. 9a, the substrate microhardness ranges from 210 to 230 HV0.3. The microhardness of the AlCoCrFeNi coating ranges from 500 to 550 HV0.3, which is 2–2.5 times that of the substrate. The transition zone thickness of the AlCoCrFeNi coating is approximately half that of the AlCoCrFeNi-Ti(C,N) coating. This may be related to the exothermic reaction between B_4C and Ti, and the excess heat leading to a larger dilution rate. The microhardness of each coating is hardly affected by the electromagnetic field since there is no formation of reinforced phases within the layers. Consequently, there is no gradient change in the microhardness of the coatings. This also proves that gradient hardness on the coating is the result of the distribution of reinforcement phase controlled by the magnetic field in the coating.

In Fig. 9b, The AlCoCrFeNi-Ti(C,N) coating is significantly influenced by the electromagnetic field. The coatings without electromagnetic field assistance exhibits higher hardness near the mushy zone and the surface, reaching approximately 650 HV0.3 and 700HV0.3, respectively. The average microhardness of AlCoCrFeNi-Ti(C,N) is about 20 % higher than that of AlCoCrFeNi, attributed to the grain refinement resulting from the in-situ synthesized reinforcing phases. In comparison to sample A, the microhardness of the coating in sample B, which is solely assisted by the magnetic field, is slightly lower but more uniform. This is due to the magnetic field restricting melt convection, resulting in larger and more uniform grains, which coincides with the microstructural analysis. Sample C exhibits a noticeable microhardness gradient, attributed to the fact that the electromagnetic force acts in the same direction as gravity. This volume force effectively increases the equivalent buoyancy within the melt pool, causing the reinforcing phases to migrate toward the surface, and forming a functionally graded coating. To eliminate the tendency of gradient changes of microhardness due to coating dilution, a comparative experiment with electromagnetic field assistance in the opposite direction of gravity is carried out to prepare sample D. The results showed higher microhardness in the transition zone near the substrate and lower microhardness in the surface layer of the coating. This leads to the conclusion that the electromagnetic

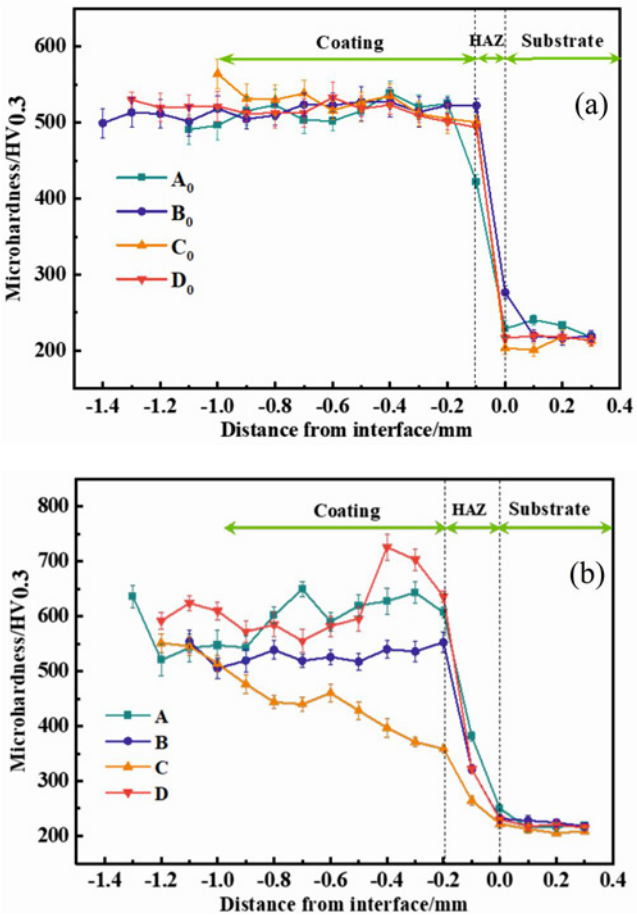

Fig. 9. Microhardness profile of coatings along the cross section: (a) microhardness profile of AlCoCrFeNi coatings and (b) microhardness profile of AlCoCrFeNi-Ti(C,N) coatings.

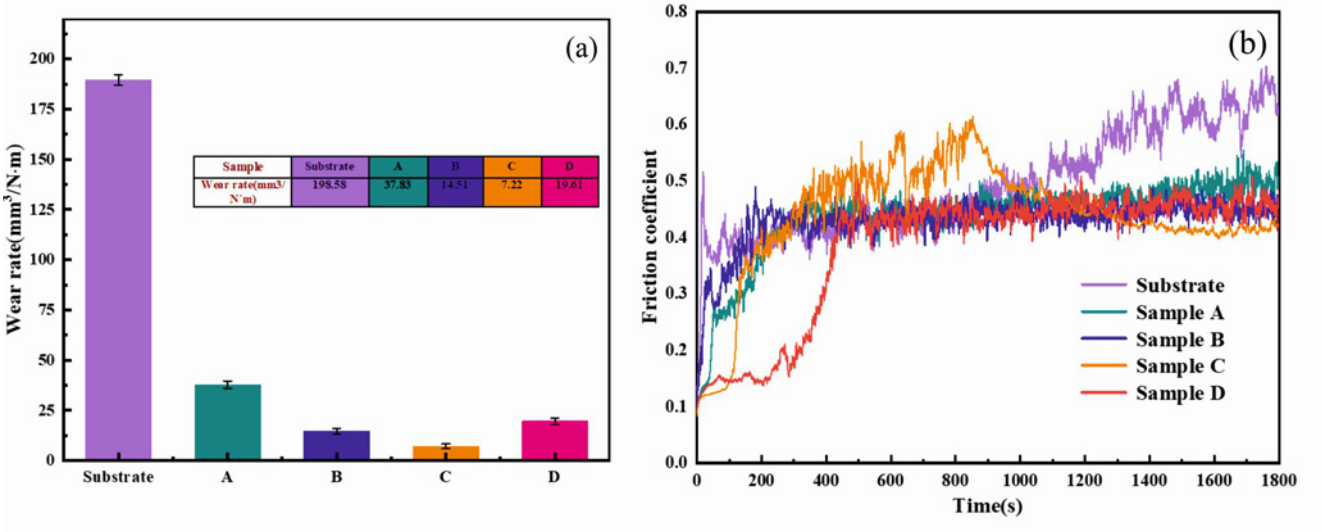

Fig. 10. Wear rate and friction coefficient of the materials: (a) comparison of wear rates and (b) comparison of friction coefficient.

field can control the distribution of in-situ synthesized reinforcing phase particles, which is consistent with theoretical predictions.

Figure 10a shows the wear rates of the coatings. Sample C, which is prepared with electromagnetic force downward assistance, exhibits the lowest wear rate, only 7.22 $mm^3\ N^{-1}\ m^{-1}$. Its wear resistance is 5.2 times that of the coating without electromagnetic field assistance. The wear rates of substrate, Samples A, B, and D were 198.58, 37.83, 14.51, and 19.61 $mm^3\ N^{-1}\ m^{-1}$, respectively. The wear rate of sample A is 2 times that of the sample B with only magnetic field assistance, and 27.5 times that of the substrate. Additionally, the sample D with electromagnetic force upward shows a higher wear rate than the coating with only magnetic field assistance. This is consistent with the expected results and with the wear mechanisms discussed previously.

Figure 10b shows the friction coefficient during the friction process for the AlCoCrFeNi-Ti(C,N) coating and the substrate. After stabilization, samples A, B, and D exhibit nearly identical friction coefficients. Among them, sample D displays the highest rate of change in friction coefficient within the first 10 minutes. This could be attributed to the initially lower Ti(N,C) content on the surface of coating D, which gradually increases with wear loss, leading to a subsequent stabilization of the friction coefficient. In contrast, sample C shows a friction coefficient curve with higher and less stable values in the early stages, followed by a gradual stabilization with the lowest friction coefficient after reaching a stable state. This observation is consistent with the wear resistance results. In summary, gradient coatings assisted by electromagnetic fields demonstrate excellent wear resistance, and this performance is correlated with the direction of the electromagnetic force.

3.3. Corrosion results

Figure 11a shows the potentiodynamic polarization results of the samples in a 3.5% NaCl solution. The coatings exhibit distinct passivation behavior during the corrosion process. Sample C and sample D prepared with electromagnetic field exhibit relatively wide passivation range, indicating that passivation film can be stable within a wider potential range. The corrosion potential (V_{corr}) and corrosion current density (I_{corr}) from fitting results are presented in Fig. 10b. The corrosion potentials for samples A, B, C, and D are –0.298, –0.303, –0.293, and –0.289 V, respectively, all of which is higher than that of the substrate (–0.328 V). The corrosion current density of sample A prepared without electromagnetic field is 1.173 $\mu A\ cm^{-2}$, while sample B with only magnetic field exhibits 44.8 % reduction in corrosion current density (0.647 $\mu A\ cm^{-2}$). The coating with electromagnetic force downward, sample C, shows 65.1% reduction in corrosion current density (0.411 $\mu A\ cm^{-2}$), while the coating with electromagnetic force upward, sample D, demonstrates 58.4 % reduction (0.499 $\mu A\ cm^{-2}$). Corrosion current density of sample C is only 12.8 % of that of the substrate. These results indicate that the coatings formed with electromagnetic field assistance are better corrosion-resistant than those without electromagnetic field assistance. Moreover, gradient coatings prepared with electromagnetic force downward exhibit the best corrosion resistance.

Figure 12 showed the electrochemical impedance

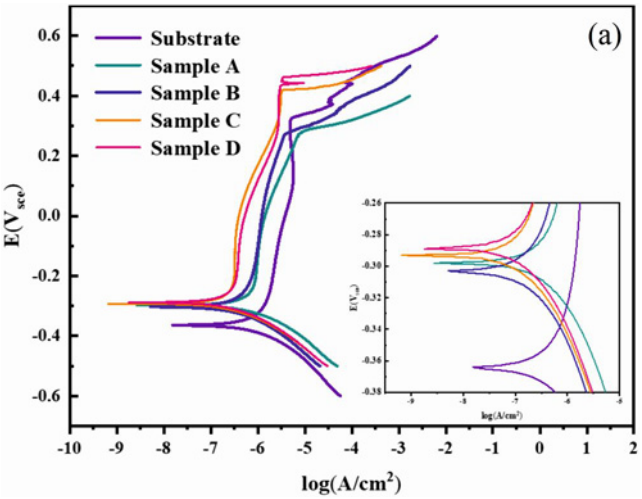

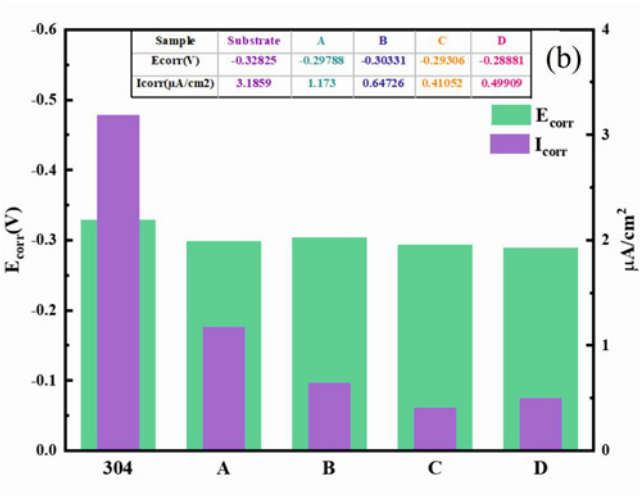

Fig. 11. Dynamic polarization results of materials in 3.5% NaCl solution: (a) potentiodynamic polarization curve and partial magnification and (b) fitting results.

spectroscopy of materials in 3.5% NaCl solution. The circular diameters for sample C, which was prepared with downward electromagnetic forces, and sample B, which was prepared only with magnetic field, are much larger than those for sample D, prepared with upward electromagnetic forces, and sample A, prepared without electromagnetic field assistance.

When electromagnetic forces are directed downward (sample C), the content of Ti(C,N) ceramic phase in the coating is higher, resulting in greater interfacial resistance with the electrolyte. Conversely, when electromagnetic forces are directed upward (sample D), Ti(C,N) is less formed on the coating's surface, leading to lower interfacial resistance compared to sample B, which is assisted only by a magnetic field. All of the Nyquist plots for coatings prepared with magnetic field exhibit larger semicircular diameters than those for coatings without magnetic assistance (sample A). This is attributed to grain refine of the coating due to the magnetic field, which is consistent with the previous structure discussed.

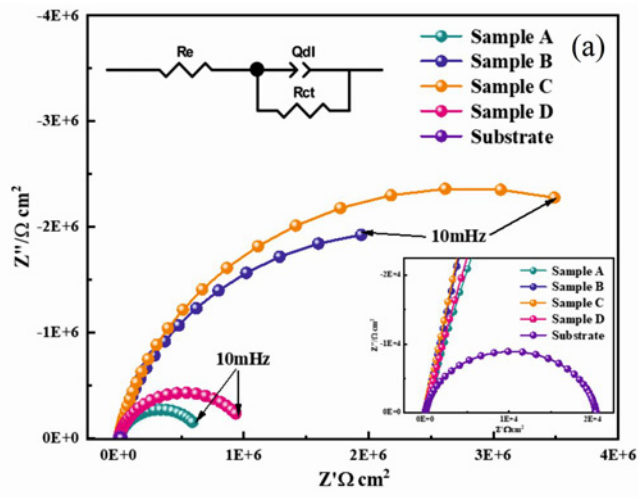

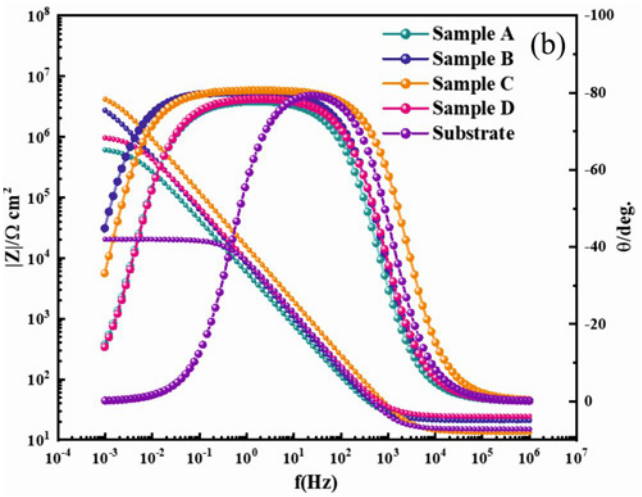

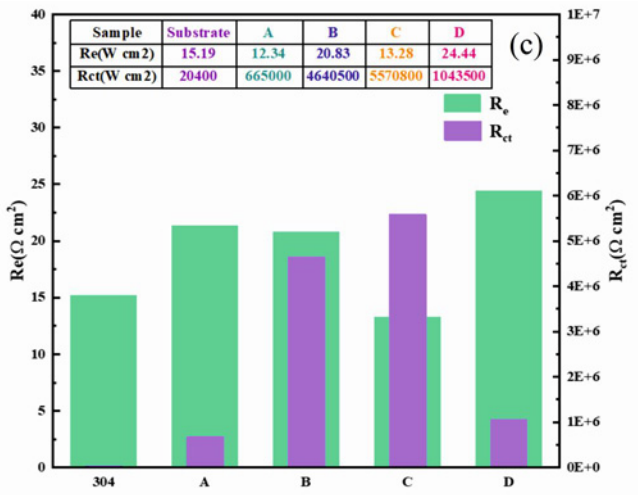

Fig. 12. Electrochemical impedance spectroscopy of materials in 3.5% NaCl solution: (a) the Nyquist and equivalent circuit, (b) bode plots, and (c) titting results.

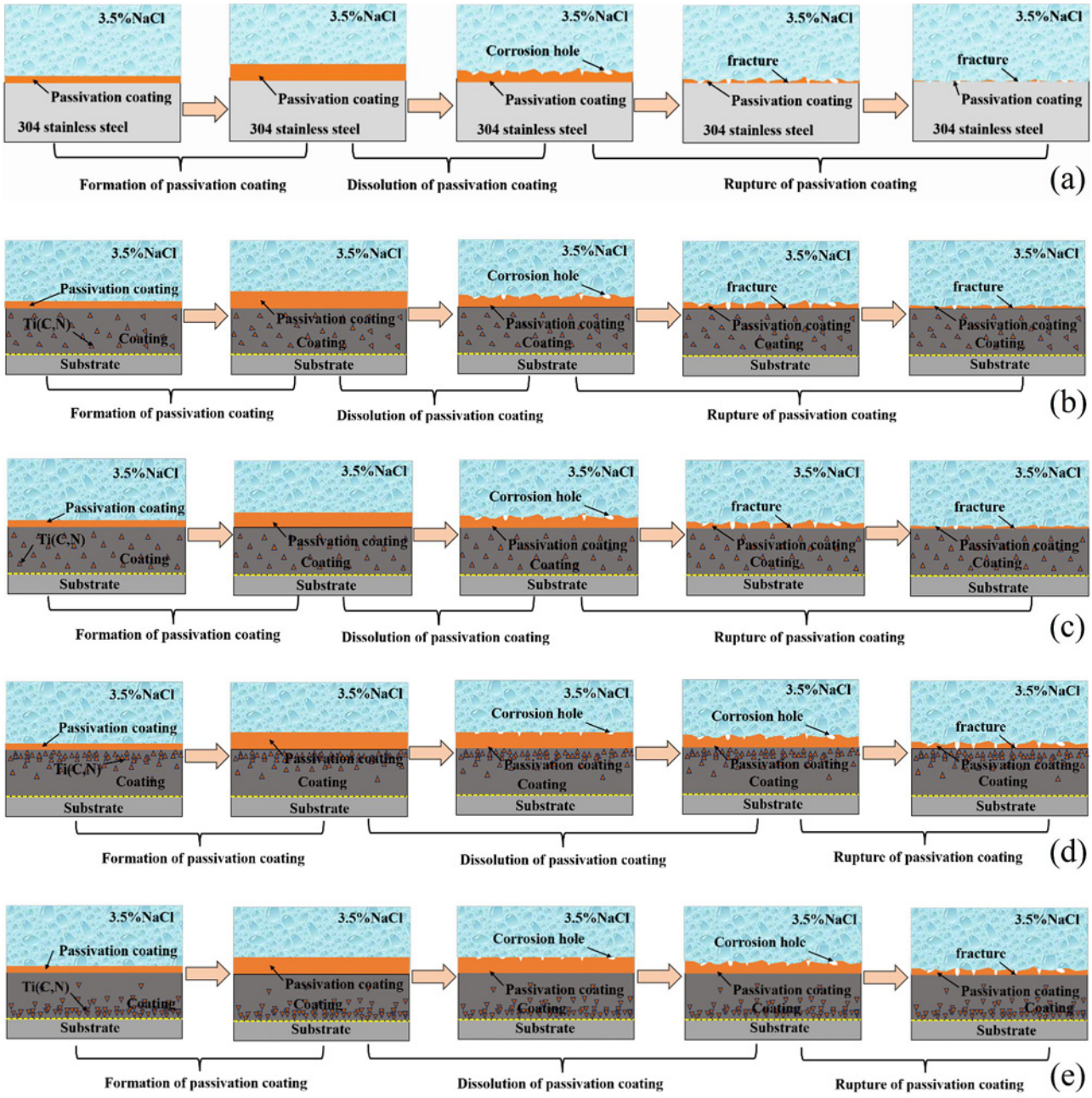

Fig. 13. Schematic diagram of corrosion process of AlCoCrFeNi-Ti(C,N) coating: (a) 304 stainless steel matrix, (b) the coating without electromagnetic field assisted, (c) the coating only with magnetic field assisted, (d) the coating with electromagnetic field assisted (electromagnetic force down), and (e) the coating with electromagnetic field assisted (electromagnetic force up).

The larger the semicircular diameter in the Nyquist plot, the better the corrosion resistance of the coating in the solution [45–48]. Therefore, the results indicate that the gradient coating, which was prepared with downward electromagnetic assistance, exhibits the highest corrosion resistance. The equivalent circuit diagram of the samples in a 3.5% NaCl solution is showed in Fig. 12a, where R_e represents the solution resistance, R_{ct} represents the charge transfer resistance, and Q_{dl} is electrical double-layer capacitor (the constant phase element, CPE). The CPE is employed to account for the non-ideal capacitive response resulting from surface uniformity, roughness, and adsorption effects [46].

The impedance of the gradient coating prepared with electromagnetic assistance (sample C) is $5.57 \times 10^6\ \Omega\,cm^2$, as shown in Fig. 12c. The impedance of sample C is significantly the highest. Therefore, the

gradient coating formed with downward-directed electromagnetic force exhibits outstanding corrosion resistance.

3.4. Corrosion mechanism model

As shown in Fig. 13, corrosion mechanism model of AlCoCrFeNi-Ti(C,N) coating is built. In the first stage, the substrate and coatings form stable passivation films with reference to the results of potential scanning analysis. In the second stage, the passivation film began to dissolve. The corrosion mechanism of the coating formed without electromagnetic field assistance and the coating formed only with magnetic field assistance, were exhibited in Figs.13b,c, whose passivation film rupture were at nearly the same potential. However, the coating formed with electromagnetic field assistance assisted exhibit wider passivation zone widths, as shown in Figs. 13d,e. Pitting corrosion occurs at higher potentials, indicating greater corrosion resistance.

4. Conclusions

In this study, AlCoCrFeNi-Ti(C,N) coatings were successfully prepared using laser cladding with electromagnetic field. These coatings exhibit excellent metallurgical bonding with the substrate, which has gradient distribution of ceramic phases within the coating. The one-step preparation of functional graded coatings simplifies the manufacturing process, and achieves energy efficiency and emission reduction objectives. This process offers a suitable solution to the issue of high-density solid ceramic particles settling in low-density metal melt pools. The main conclusions are summarized as follows:

(1) When the electromagnetic force direction is parallel to gravity, the FCC phase exhibits orientation and the BCC phase forms a continuous structure. The microhardness of AlCoCrFeNi-Ti(C,N) coatings gradually increases from the substrate to the surface, reaching its maximum value at the surface.

(2) When the electromagnetic force direction is opposite to gravity, it enhances the directionality of the FCC phase and leads to a honeycomb-like structure. The upward electromagnetic force inhibits the formation of the BCC phase. This leads to the maximum microhardness occurring near the substrate-coating interface, with an overall trend of increasing microhardness from the substrate to the coating surface.

(3) The introduction of an electromagnetic field significantly enhances the wear resistance of the gradient coating, particularly when the electromagnetic force is directed downwards. The coating exhibits the best wear resistance.

(4) The gradient coatings exhibit excellent corrosion resistance in a 3.5% NaCl solution. Corrosion resistance is almost 2.8 times the coatings prepared without electromagnetic field and about 7.8 times the substrate.

Acknowledgements

This work was supported by Special Fund for Basic Research Business Expenses of Zhongyuan University of Technology(K2020YY004), Henan Province Science and Technology Research Project (252102221051, 252102231020), Key Scientific Research Projects of Henan Province (25A510001), International Science and Technology Cooperation Project of Henan Province (242102520005), General Project of Education Science Planning in Henan Province (2024YB0516), and Nanyang Basic and Frontier Technology Research Special Project (23JCQY2022).

References

[1] B. Cantor, I. T. H. Chang, P. Knight, A. J. B. Vincent, Microstructural development in equiatomic multicomponent alloys, Mater. Sci. Eng. A 375 (2004) 213–218. https://doi.org/10.1016/j.msea.2003.10.257

[2] J. W. Yeh, S. K. Chen, S. J. Lin, Y. Gan, T. S. Chin, T. T. Shun, C. H. Tsau, S. Y. Chang, Nanostructured high-entropy alloys with multiple principal elements: Novel alloy design concepts and outcomes, Adv. Eng. Mater. 6 (2004) 299–303. https://doi.org/10.1002/adem.200300567

[3] N. D. Stepanov, D. G. Shaysultanov, N. Y. Yurchenko, S. V. Zherebtsov, A. N. Ladygin, G. A. Salishchev, M. A. Tikhonovsky, High temperature deformation behavior and dynamic recrystallization in CoCrFeNiMn high entropy alloy, Mater. Sci. Eng.: A 636 (2015) 188–195. https://doi.org/10.1016/j.msea.2015.03.097

[4] N. Li, S. Wu, D. Ouyang, J. Zhang, L. Liu, Fe-based metallic glass reinforced FeCoCrNiMn high entropy alloy through selective laser melting, J. Alloy. Compd. 822 (2020) 153695. https://doi.org/10.1016/j.jallcom.2020.153695

[5] H. Cheng, Y. Fang, J. Xu, C. Zhu, P. Dai, S. Xue, Tribological properties of nano/ultrafine-grained $FeCoCrNiMnAl_X$ high-entropy alloys over a wide range of temperatures, J. Alloy. Compd. 817 (2020) 153305. https://doi.org/10.1016/j.jallcom.2019.153305

[6] E. P. George, W. A. Curtin, C. C. Tasan, High entropy alloys: A focused review of mechanical properties and deformation mechanisms, Acta Mater. 188 (2020) 435–474. https://doi.org/10.1016/j.actamat.2019.12.015

[7] Y. Guo, H. Su, P. Yang, Y. Zhao, Z. Shen, Y. Liu, L. Lin H. Fu, A review of emerging metallic system for high-energy beam additive manufacturing: Al-Co-Cr-Fe-Ni high entropy alloys, Acta Metall. Sin. (Engl. Lett.) 35 (2022) 1407–1423. https://doi.org/10.1007/s40195-022-01400-y

[8] L. Zhu, P. Xue, Q. Lan, G. Meng, Y. Ren, Z. Yang, P. Xu, Z. Liu, Recent research and development status of laser cladding: A review, Opt. Laser Technol. 138

(2021) 106915.
https://doi.org/10.1016/j.optlastec.2021.106915
[9] Y. Liu, Y. Ding, L. Yang, R. Sun, T. Zhang, X. Yang, Research and progress of laser cladding on engineering alloys: A review, J. Manuf. Process 66 (2021) 341–363. https://doi.org/10.1016/j.jmapro.2021.03.061
[10] W. R. Wang, W. L. Wang, S. C. Wang, T. C. Tsai, C. H. Lai, J. W. Yeh, Effects of Al addition on the microstructure and mechanical property of $Al_xCoCrFeNi$ high-entropy alloys, Intermetallics, 26 (2012) 44–51. https://doi.org/10.1016/j.intermet.2012.03.005
[11] I. Kunce, M. Polanski, K. Karczewski, T. Plocinski, K. J. Kurzydlowski, Microstructural characterisation of high-entropy alloy AlCoCrFeNi fabricated by laser engineered net shaping, J. Alloy. Compd. 648 (2015) 751–758. https://doi.org/10.1016/j.jallcom.2015.05.144
[12] R. Wang, K. Zhang, C. Davies, X. Wu, Evolution of microstructure, mechanical and corrosion properties of AlCoCrFeNi high-entropy alloy prepared by direct laser fabrication, J. Alloy. Compd. 694 (2017) 971–981. https://doi.org/10.1016/j.jallcom.2016.10.138
[13] Y.F. Juan, J. Li, Y.Q. Jiang, W. L. Jia, Z. J. Lu, Modified criterions for phase prediction in the multi-component laser-clad coatings and investigations into microstructural evolution/wear resistance of FeCrCoNiAlMox laser-clad coatings, Appl. Surf. Sci. 465 (2019) 700–714. https://doi.org/10.1016/j.apsusc.2018.08.264
[14] W. Muftah, J. Allport, V. Vishnyakov, Corrosion performance and mechanical properties of FeCrSiNb amorphous equiatomic HEA thin film, Surf. Coat. Technol. 422 (2021) 127486. https://doi.org/10.1016/j.surfcoat.2021.127486
[15] H. Liu, J. Liu, X. I. Li, P. Chen, H. Yang, J. Hao, Effect of heat treatment on phase stability and wear behavior of laser clad AlCoCrFeNiTi0.8 high-entropy alloy coatings, Surf. Coat. Technol. 392 (2020) 125758. https://doi.org/10.1016/j.surfcoat.2020.125758
[16] Y. Li, K. Wang, H. Fu, X. Guo, J. Lin, Microstructure and wear resistance of in-situ TiC reinforced AlCoCrFeNi-based coatings by laser cladding, Appl. Surf. Sci. 585 (2022) 152703. https://doi.org/10.1016/j.apsusc.2022.152703
[17] X. Li, Y. Feng, B. Liu, D. Yi, X. Yang, W. Zhang, G. Chen, Y. Liu, P. Bai, Influence of NbC particles on microstructure and mechanical properties of AlCoCrFeNi high-entropy alloy coatings prepared by laser cladding, J. Alloy. Compd. 788 (2019) 485–494. https://doi.org/10.1016/j.jallcom.2019.02.223
[18] S. Ma, Y. Zhang, Effect of Nb addition on the microstructure and properties of AlCoCrFeNi high-entropy alloy, Mater. Sci. Eng. A 532 (2012) 480–486. https://doi.org/10.1016/j.msea.2011.10.110
[19] Y. T. Pei, D. Galvan, J. T. M. De Hosson, Nanostructure and properties of TiC/a-C: H composite coatings, Acta Mater. 53 (2005) 4505–4521. https://doi.org/10.1016/j.actamat.2005.05.045
[20] I. A. Ibrahim, F. A. Mohamed, E. J. Lavernia, Particulate reinforced metal matrixc composite-A review, J. Mater. Sci. 26 (1991) 1137–1156. https://doi.org/10.1007/BF00544448
[21] W. Lengauer, Transition Metal Carbides, Nitrides, and Carbonitrides. in: R. Riedel (Ed.), Handbook of Ceramic Hard Materials, Wiley, Weinheim, 2000, pp. 202–252. https://doi.org/10.1002/9783527618217.ch7
[22] S. Oukach, B. Pateyron, L. Pawłowski, Physical and chemical phenomena occurring between solid ceramics and liquid metals and alloys at laser and plasma composite coatings formation: A review, Surf. Sci. Rep. 74 (2019) 213–241. https://doi.org/10.1016/j.surfrep.2019.06.001
[23] S. C. Tjong, Z. Y. Ma, Microstructural and mechanical characteristics of in situ metal matrix composites, Mater. Sci. Eng. R Rep. 29 (2000) 49–113. https://doi.org/10.1016/S0927-796X(00)00024-3
[24] L. Chen, Y. Chen, X. Chen, T. Yu, Z. Wang, Microstructure and properties of in situ TiC/Ni functionally gradient coatings by powder-fed laser cladding, Ceram. Int. 48 (2022) 36789–36801. https://doi.org/10.1016/j.ceramint.2022.08.243
[25] X. Wang, Z. Zhang, Y. Men, X. Li, Y. Liang, L. Ren, Fabrication of nano-TiC functional gradient wear-resistant composite coating on 40Cr gear steel using laser cladding under starved lubrication conditions, Opt. Laser Technol. 126 (2020) 106136. https://doi.org/10.1016/j.optlastec.2020.106136
[26] G. Yan, M. Zheng, Z. Ye, J. Gu, C. Li, C. Wu, B. Wang, In-situ Ti (C, N) reinforced AlCoCrFeNiSi-based high entropy alloy coating with functional gradient double-layer structure fabricated by laser cladding, J. Alloy. Compd. 886 (2021) 161252. https://doi.org/10.1016/j.jallcom.2021.161252
[27] Z. Zhao, Y. Chai, S. Zheng, L. Wang, Y. Xiao, Electromagnetic field assisted metallic materials processing: A review, Steel Res. Int. 88 (2017) 1600273. https://doi.org/10.1002/srin.201600273
[28] K. Iwai, J. Akiyama, M. G. Sung, I. Furuhashi, S. Asai, Application of a strong magnetic field on materials fabrication and experimental simulation, Sci. Technol. Adv. Mater. 7 (2006) 365–368. https://doi.org/10.1016/j.stam.2006.01.011
[29] Z. H. I. Sun, M. Guo, J. Vleugels, O. Van der Biest, B. Blanpain, Strong static magnetic field processing of metallic materials: A review, Curr. Opin. Solid State Mater. Sci. 16 (2012) 254–267. https://doi.org/10.1016/j.cossms.2012.08.001
[30] C. J. Song, Z. Xu, J. G. Li, In-situ Al/Al3Ni functionally graded materials by electromagnetic separation method, Mater. Sci. Eng. A 445 (2007) 148–154. https://doi.org/10.1016/j.msea.2006.09.009
[31] C. Song, Z. Xu, J. Li, Structure of in situ Al/Si functionally graded materials by electromagnetic separation method, Mater. Des. 28(3) (2007) 1012–1015. https://doi.org/10.1016/j.matdes.2005.11.007
[32] C. Song, Z. Xu, X. Liu, G. Liang, J. Li, In situ multilayer functionally graded materials by Electromagnetic Separation method, Materials Science and Engineering: A 393 (2005) 164–169. https://doi.org/10.1016/j.msea.2004.10.006
[33] K. Huo, J. Zhou, F. Dai, J. Xu, Particle distribution and microstructure of IN718/WC composite coating fabricated by electromagnetic compound field-assisted laser cladding, Appl. Surf. Sci. 545 (2021) 149078. https://doi.org/10.1016/j.apsusc.2021.149078
[34] L. Wang, J. Yao, Y. Hu, Q. Zhang, Z Sun, R. Liu, Influence of electric-magnetic compound field on the WC particles distribution in laser melt injection, Surf.

Coat. Technol. 315 (2017) 32–43. https://doi.org/10.1016/j.surfcoat.2017.01.116
[35] L. C. Cao, D. H Liu, P. Jiang, X. Sha, Q. Zhou, Y. Wang, Multi-physics simulation of dendritic growth in magnetic field assisted solidification, Int. J. Heat Mass Transf. 144 (2019) 118673.https://doi.org/10.1016/j.ijheatmasstransfer.2019.118673
[36] A. Manzoni, H. Daoud, R. Völkl, U. Glatzel, N. Wanderka, Phase separation in equiatomic AlCoCrFeNi high-entropy alloy, Ultramicroscopy, 132 (2013) 212–215. https://doi.org/10.1016/j.ultramic.2012.12.015
[37] A. Munitz, S. Salhov, S. Hayun, N. Frage, Heat treatment impacts the micro-structure and mechanical properties of AlCoCrFeNi high entropy alloy, J. Alloy. Compd. 683 (2016) 221–230. https://doi.org/10.1016/j.jallcom.2016.05.034
[38] W. R. Wang, W. L. Wang, J. W. Yeh, Phases, microstructure and mechanical properties of Al_xCoCrFeNi high-entropy alloys at elevated temperatures, J. Alloy. Compd. 589 (2014) 143–152. https://doi.org/10.1016/j.jallcom.2013.11.084
[39] Y. Q. Jiang, J. Li, Y. F. Juan, Z. J. Lu, W. L. Jia, Evolution in microstructure and corrosion behavior of $AlCoCr_xFeNi$ high-entropy alloy coatings fabricated by laser cladding, J. Alloy. Compd. 775 (2019) 1–14. https://doi.org/10.1016/j.jallcom.2018.10.091
[40] L. Guo, D. Xiao, W. Wu, S. Ni, M. Song, Effect of Fe on microstructure, phase evolution and mechanical properties of $(AlCoCrFeNi)_{100-x}Fe_x$ high entropy alloys processed by spark plasma sintering, Intermetallics, 103 (2018) 1–11. https://doi.org/10.1016/j.intermet.2018.09.011
[41] T. M. Butler, M. L. Weaver, Oxidation behavior of arc melted AlCoCrFeNi multicomponent high-entropy alloys, J. Alloy. Compd. 674 (2016) 229–244. https://doi.org/10.1016/j.jallcom.2016.02.257
[42] B. Du, Z. Zou, X. Wang, S. Qu, Laser cladding of in situ TiB2/Fe composite coating on steel, Appl. Surf. Sci. 254 (2008) 6489–6494. https://doi.org/10.1016/j.apsusc.2008.04.051
[43] G. Liang, G. Jin, X. Cui, Z. Qiu, J. Wang, The directional array TiN-reinforced AlCoCrFeNiTi high-entropy alloy synthesized in situ via magnetic field-assisted laser cladding, Appl. Surf. Sci. 572 (2022) 151407. https://doi.org/10.1016/j.apsusc.2021.151407
[44] X. Tan, Y. Tan, Y. Tang, S. Suna, S. Zhang, H. Xua, The improvement of magnetic property by grain refinement using magnetic field annealing crystalline $(Nd_{0.8}Pr_{0.2})_{2.2}Fe_{12}Co_2B$ ribbons, J. Magn. Magn. Mater. 518 (2021) 167434. https://doi.org/10.1016/j.jmmm.2020.167434
[45] A. B. Oliveira, A. C. Bastos, C. M. Fernandes, C. M. S. Pinho, A. M. R. Senos, E. Soares, J. Sacramento, M. L. Zheludkevich, M. G. S. Ferreira, Corrosion behaviour of WC-10% AISI 304 cemented carbides, Corros. Sci. 100 (2015) 322–331. https://doi.org/10.1016/j.corsci.2015.08.006
[46] L. Wei, Y. Liu, Q. Li, J. F. Cheng, Effect of roughness on general corrosion and pitting of (FeCoCrNi)0.89(WC)0.11 high-entropy alloy composite in 3.5 wt.% NaCl solution, Corros. Sci. 146 (2019) 44–57. https://doi.org/10.1016/j.corsci.2018.10.025
[47] J. Wang, W. Li, H. Yang, H. Huang, S. Ji, J. Ruan, Z. Liu, Corrosion behavior of CoCrNi medium-entropy alloy compared with 304 stainless steel in H_2SO_4 and NaOH solutions, Corros. Sci. 177 (2020) 108973. https://doi.org/10.1016/j.corsci.2020.108973
[48] C. N. Cao, On the impedance plane displays for irreversible electrode reactions based on the stability conditions of the steady-state-I. One state variable besides electrode potential, Electrochim. Acta, 35 (1990) 831–836. https://doi.org/10.1016/0013-4686(90)90077-D